Volume 17
Number 8
25 February 2026
Pages 3861–4348

Chemical Science

rsc.li/chemical-science

ISSN 2041-6539

ROYAL SOCIETY OF CHEMISTRY

EDGE ARTICLE

Jiří Kaleta *et al.*

Cucurbit[7]uril as a universal anchor for photoswitchable monolayers on gold

Chemical Science

ROYAL SOCIETY OF CHEMISTRY

EDGE ARTICLE

View Article Online
View Journal | View Issue

Cite this: *Chem. Sci.*, 2026, **17**, 3991

All publication charges for this article have been paid for by the Royal Society of Chemistry

Received 3rd December 2025
Accepted 11th January 2026

DOI: 10.1039/d5sc09469k

rsc.li/chemical-science

Cucurbit[7]uril as a universal anchor for photoswitchable monolayers on gold

Doroteja Lončarić,[ab] Eva Kaletová,[a] Katarina Majerová Varga,[a] Carina Santos Hurtado,[a] Milan Mašát,[a] Ivana Císařová[b] and Jiří Kaleta *[a]

Photoresponsive self-assembled monolayers (SAMs) were fabricated on gold surfaces using cucurbit[7]uril (**CB[7]**)-based host–guest complexes. In this architecture, the macrocyclic **CB[7]** unit serves as a universal anchoring platform, with one portal binding to the gold surface and the opposite portal encapsulating a photoswitchable molecular rod featuring a pyridinium–adamantyl recognition site. Four distinct molecular rods were synthesized to demonstrate the versatility of this modular approach. In solution, all supramolecular complexes retained the inherent photoresponsive behavior of the parent rods, exhibiting reversible isomerization with high fatigue resistance and minimal perturbation from **CB[7]** complexation. Upon surface immobilization, the resulting monolayers retained functional photoactivity, as demonstrated on all four systems. These results underscore the potential of **CB[7]**-anchored assemblies for the fabrication of robust, light-responsive surfaces and molecular devices.

Introduction

The development of functionalized two-dimensional (2-D) surfaces is central to advancing molecular electronics, sensing, and responsive materials.[1–6] These systems typically consist of self-assembled monolayers (SAMs) where the constituent molecules feature three critical elements: a functional headgroup (*e.g.*, photoswitch or molecular motor), a linker, and a surface-anchoring unit. While the headgroup is generally transferable between different systems, the design of the linker and anchoring moieties must be carefully tailored to suit the characteristics of specific substrates, such as metallic *versus* non-metallic surfaces, or solid *versus* liquid interfaces.[2] These non-functional segments are not merely structural supports: they play a crucial role in orienting the headgroup, decoupling it electronically from the substrate, allowing sufficient conformational freedom for switching, and preventing intermolecular quenching or energy transfer.[2] If improperly designed, they can dramatically impair or completely disable the functionality of the molecular layer.

Despite extensive development of surface functionalization strategies,[7–15] challenges remain. Many such approaches involve multistep syntheses and lack modularity, making them less adaptable to diverse molecular functions or new substrate types. To address these limitations, supramolecular methods based on non-covalent interactions have emerged as promising alternatives. In particular, host–guest interactions offer a unique combination of high affinity, selectivity, and reversibility, enabling the construction of modular, tunable, and dynamic molecular architectures.[16–21]

Herein, we present a supramolecular strategy for constructing light-responsive SAMs on gold surfaces using host–guest complexes formed between rod-like molecules **1–4** and the macrocyclic host cucurbit[7]uril (**CB[7]**) (Fig. 1). This approach exploits the known ability of **CB[7]** to physisorb onto gold surfaces *via* one of its portals, effectively acting as a universal anchoring unit or a molecular pedestal.[22–25] To complement this, guest molecules were designed with an adamantyl–pyridinium recognition site that strongly binds within the **CB[7]** cavity (for reference, the closely related *N*-(1-adamantyl)pyridinium bromide binds **CB[7]** with $K_a = (1.98 \pm 0.42) \times 10^{12}$ M^{-1} in aqueous buffer),[26] allowing the remainder of the molecule to protrude from the host while the opposite portal of **CB[7]** remains available for surface anchoring.

To demonstrate the modularity and functional scope of this platform, we incorporated the binding motif into four representative molecular systems: a light-driven molecular motor **1** and three photoswitches **2–4**. The formation of discrete 1:1 host–guest complexes **1–4**·**CB[7]** in solution was confirmed, and their fundamental photochemical properties were characterized. These complexes were then immobilized onto gold surfaces to form SAMs, which were investigated using ellipsometry, contact angle measurements, polarization modulation infrared reflection–absorption spectroscopy (PM-IRRAS), and surface-enhanced Raman spectroscopy (SERS). Crucially, the photoresponsive behavior of the guest molecules was retained on the surface, demonstrating that this **CB[7]**-based

[a]*Institute of Organic Chemistry and Biochemistry of the Czech Academy of Sciences, Flemingovo nám. 2, 160 00 Prague 6, Czech Republic. E-mail: jiri.kaleta@uochb.cas.cz*
[b]*Department of Inorganic Chemistry, Faculty of Science, Charles University Prague, Hlavova 2030, 128 40 Prague 2, Czech Republic*

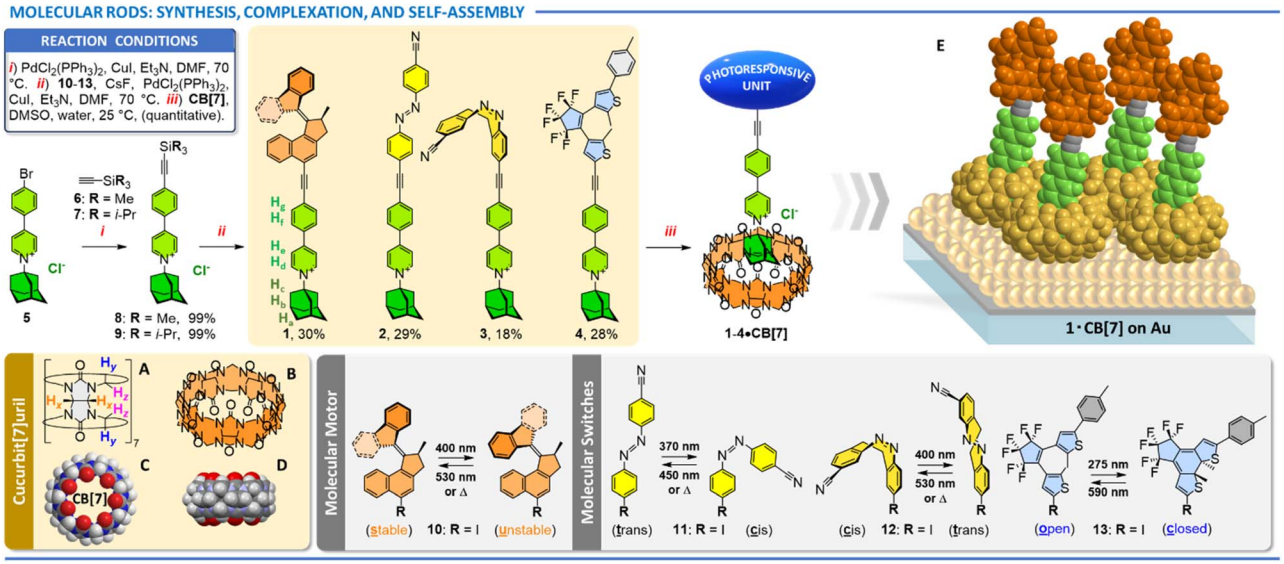

Fig. 1 Synthesis of molecular rods **1–4** and their reaction with **CB[7]** leading to supramolecular complexes **1–4·CB[7]**. **CB[7]**: a schematic representation (A), chemical structure (B), and top (C) and side (D) view on a space-filling model. Idealized visualization of **1·CB[7]** on a gold surface (E).

supramolecular platform can be used to create robust, light-active monolayers with high modularity and functional fidelity.

Results and discussion

The molecular rods **1–4** were synthesized through two consecutive Sonogashira cross-coupling reactions, starting from the previously reported adamantylated pyridinium **5** (Fig. 1). In the first step, bromine was formally substituted with ethynyltrimethylsilane (**6**) or ethynyltriisopropylsilane (**7**), yielding the silyl-protected derivatives **8** and **9** in excellent yields. While both intermediates successfully led to the desired products in subsequent reactions, **9** exhibited greater stability during purification and long-term storage. The final step involved the *in situ* removal of the silyl protecting group using CsF, followed by cross-coupling with iodides **10–13**, affording the target compounds in nearly quantitative yield (as determined by ^{1}H NMR of the crude reaction mixture). However, the isolated yields were approximately 25%, reflecting the challenges of separating poorly soluble cationic species from complex reaction mixtures. Interestingly, all attempts to isolate the intermediate terminal acetylene failed, as its removal of silyl groups consistently led to quantitative oxidative homocoupling, preventing isolation of the desired product.

Supramolecular complexes **1–4·CB[7]** were quantitatively obtained in preparative quantities through a stoichiometric reaction between **1–4** and **CB[7]** in DMSO (Fig. 1). Encapsulation was monitored using ^{1}H NMR spectroscopy and progress of representative titration was demonstrated on the most symmetric derivative **2** (Fig. 2). Titration data for the remaining complexes are provided in the SI.

The attachment of the **CB[7]** unit resulted in a noticeable upfield shift of the adamantyl hydrogen atoms (H_a-H_c) as well as both resonances of the pyridinium moiety (H_d and H_e). The shielding effect on other hydrogen atoms progressively diminished with increasing distance from the **CB[7]** unit, clearly indicating that only the adamantylated pyridinium serves as the binding site.

It is worth noting that **1–4·CB[7]** were accompanied by a small but detectable amounts of alkali or alkaline-earth metal-promoted trimers.[27] Their presence does not interfere with subsequent reaction, as these species are stable only in non-aqueous environments. The overall binding affinity of structurally related compound with the analogous binding site to **CB[7]** in DMSO was previously determined to be 10^4 M^{-1} using UV-vis spectroscopy.[26]

The thermal stability of the selected supramolecular complexes **1–2·CB[7]**, as well as their individual components - the free rods **1** and **2** and the **CB[7]** macrocycle - was evaluated

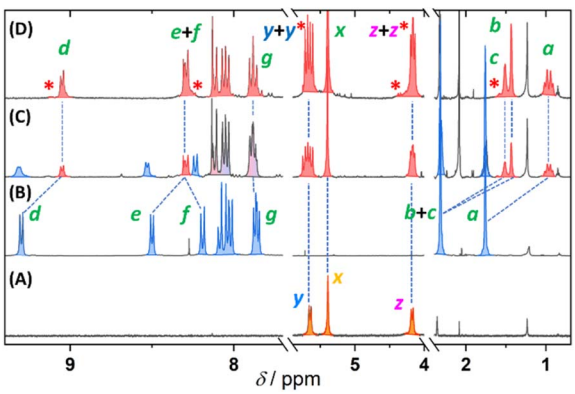

Fig. 2 ^{1}H NMR spectra of **CB[7]** (A), **2** (c = 10 mmol L^{-1}) (B), **2** with addition of 0.5 equiv. (C) and 1.0 equiv. (D) of **CB[7]** recorded in DMSO-d_6 at 25 °C. Green asterisks indicate alkali or alkaline-earth metal-promoted trimers. See Fig. 1 for atom labelling.

using differential scanning calorimetry (DSC). Pronounced endothermic transitions observed above 300 °C are attributed to the melting of the samples (Fig. 3). Notably, the melting points of the complexes were higher than those of the free guests and the **CB[7]** macrocycle, suggesting enhanced solid-state stability resulting from host–guest complexation.

Although crystal structures of one intermediate (compound **8**) and one molecular rod (compound **2** in Fig. 4) were successfully obtained, all attempts to crystallize the final complexes were unsuccessful. As a practical and informative alternative, computational modelling was employed to access the desired geometries. The structures of complexes **1–4·CB[7]** were optimized using the GFN2-xTB semi-empirical method.[28–30] Fig. 4 presents **2·CB[7]** as a representative example, while the remaining structures are provided in the SI.

In all optimized geometries, the principal molecular axis defined by the triple bonds was tilted by approximately 18° from the normal to the plane formed by the **CB[7]** oxygen atoms on one portal. These findings are consistent with previous observations made for structurally related systems.[31]

A detailed characterization of the photoswitching behavior in solution was essential before undertaking any photochemical experiments on surfaces. Additionally, it was important to assess whether the switching properties of compounds **1–4** are affected by supramolecular complexation. The proper operation of the light-driven molecular motors and photoswitches, both in the free rods **1–4** and in the supramolecular complexes **1–4·CB[7]**, was therefore independently evaluated using UV-vis and ^{1}H NMR spectroscopies in DMSO. The well-soluble functional headgroups **10–13** were analyzed in chloroform. UV-vis absorption spectra of supramolecular complexes **1–4·CB[7]** (c = 1.3–2.8 × 10^{-5} mol L^{-1}) were recorded in the presence of an excess of **CB[7]** ($c \approx 1$ mmol L^{-1}) to ensure complete complexation of the molecular rods. Fig. 5 displays the spectra for photochromic **4**, which exhibited the most pronounced

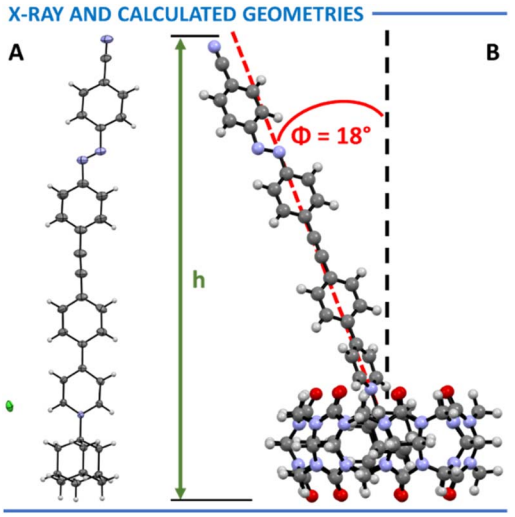

Fig. 4 ORTEP representation of molecular rod **2** with thermal ellipsoids displayed at the 30% probability level (A). Gas-phase optimized structure of **2·CB[7]** (B). Color scheme: hydrogen = white, carbon = grey, nitrogen = blue, oxygen = red, chlorine = green.

spectral changes upon photoisomerization. UV-vis spectra for the remaining complexes are provided in the SI.

Basic kinetic parameters like enthalpy ($\Delta H^{\neq}$) and Gibbs free energy of activation ($\Delta G^{\neq}$), together with a half-life at 20 °C ($t_{1/2}$) and a corresponding rate constant (k^0) characterizing thermal steps of photoswitches and motors are summarized in Table 1. Detailed description of individual systems is provided in the SI.

All systems showed fully reversible switching and rods **1–3** along with complexes **1–3·CB[7]** and precursors **10–12** also excellent fatigue resistance since almost no decomposition was detected after more than 10 irradiation cycles. In contrast, compounds **4**, **4·CB[7]**, and **13** showed reduced stability, with photoswitching accompanied by evident photobleaching.

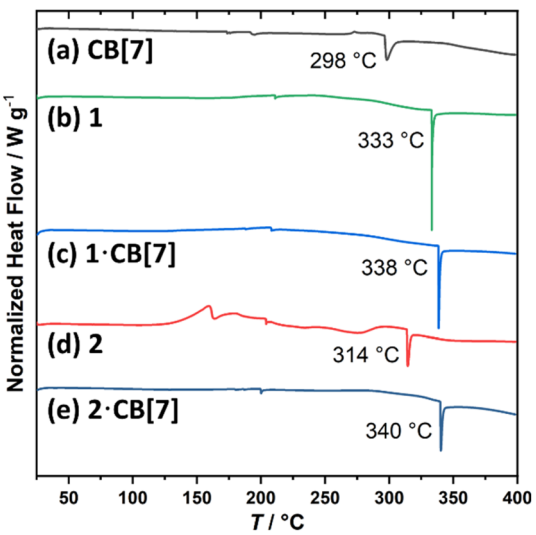

Fig. 3 DSC traces of (a) **CB[7]**, (b) **1**, (c) **1·CB[7]**, (d) **2** and (e) **2·CB[7]** from 25 to 350 °C, scanned at 10 °C min^{-1}, with labelled melting points.

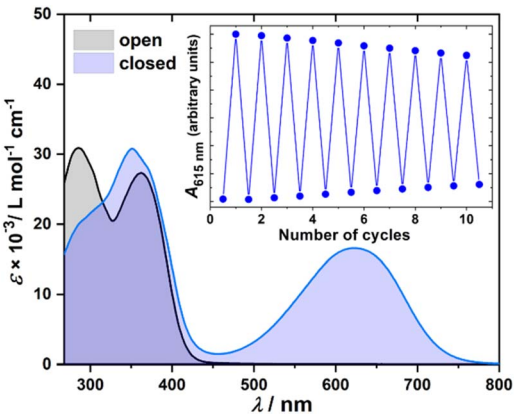

Fig. 5 UV-vis spectra of **4** (c = 2.6 × 10^{-5} mol L^{-1}) in DMSO: before irradiation (solid black line) and in PSS (solid blue line) reached after **4** minutes of irradiation with 308 ± 5 nm light; insert: absorbance of **4** (c = 2.6 × 10^{-5} mol L^{-1}) in acetonitrile at 615 nm after subsequent cycles of irradiation with 275 ± 5 nm light (6 min) and 590 ± 5 nm light (6 min).

Table 1 Photostationary states (PSS), enthalpy ($\Delta H^{\ddagger}$) and Gibbs free energy of activation ($\Delta G^{\ddagger}$), rate constants (k^0), and half-life ($t_{1/2}$) of rods **1–4** and complexes **1–4·CB[7]** determined in DMSO and within SAMs, along with corresponding values for functional headgroups **10–13** in chloroform

			Kinetic parameters			
Cmpd[a]	Irrad. (nm)	PSS[b]	$\Delta H^{\ddagger}$ (kJ mol^{-1})	$\Delta G^{\ddagger}$ (kJ mol^{-1})	k^0 (s^{-1})	$t_{1/2}$[c]
1	400	—[d]	79 ± 1	86 ± 1	2.8 ± 0.4 × 10^{-3}	4.3 ± 0.6 min
2	370	74:26	99 ± 3	101 ± 1	6.9 ± 1.4 × 10^{-6}	28 ± 6 h
3	400	50:50	97 ± 2	95 ± 2	8.2 ± 0.4 × 10^{-5}	140 ± 5 min
4	275	5:95	—[e]	—[e]	—[e]	—[e]
1·CB[7]	400	—[d]	89 ± 1	87 ± 1	2.3 ± 0.1 × 10^{-3}	5.1 ± 0.2 min
1·CB[7] (SAM)	400	—[f]	109 ± 19	86 ± 38	2.8 ± 0.8 × 10^{-3}	4.1 ± 1.2 min
2·CB[7]	370	n.d	101 ± 1	101 ± 1	6.6 ± 0.6 × 10^{-6}	29 ± 3 h
2·CB[7] (SAM)	370	—[f]	127 ± 14	101 ± 30	5.9 ± 1.7 × 10^{-6}	33 ± 9 h
3·CB[7]	400	n.d	103 ± 1	95 ± 1	7.0 ± 0.3 × 10^{-5}	164 ± 7 min
3·CB[7] (SAM)	400	—[f]	93 ± 52	80 ± 26	1.5 ± 0.8 × 10^{-5}	76 ± 41 min
4·CB[7]	275	5:95	—[e]	—[e]	—[e]	—[e]
10	400	15:85	87 ± 1	87 ± 1	1.9 ± 0.4 × 10^{-3}	6 ± 1 min
11	370	23:77	104 ± 2	102 ± 2	3.7 ± 0.7 × 10^{-6}	52 ± 10 h
12	400	18:82	101 ± 1	96 ± 1	4.6 ± 0.2 × 10^{-5}	257 ± 13 min
13	275	1:99	—[e]	—[e]	—[e]	—[e]

[a] Compounds **1–4** and their **CB[7]** complexes **1–4·CB[7]** were analyzed in DMSO, whereas compounds **10–13** were analyzed in chloroform. [b] Photostationary states (PSS) achieved at defined wavelengths as determined by ^{1}H NMR. [c] Half-life ($t_{1/2}$) of thermal reactions reported at 20 °C. [d] The value could not be determined because the required irradiation time exceeded the thermal half-life, and the sample could not be cooled due to DMSO freezing. [e] The value is not available, as the compound does not undergo thermal switching. [f] PSS was not determined for surface-adsorbed switches and motor.

The following conclusions can be drawn from the experimentally determined kinetic parameters. The overcrowded alkene-based molecular motors **1**, **1·CB[7]**, and **10** exhibited half-lives of approximately 5 minutes, whereas the azobenzene derivatives **2**, **2·CB[7]**, and **11** showed significantly longer half-lives of about 1–2 days. In contrast, the diazocine-based systems **3**, **3·CB[7]**, and **12** demonstrated intermediate half-lives in the range of 2–4 hours at 20 °C. Notably, the iodinated precursors **10–12** displayed longer half-lives than their corresponding derivatives **1–3** and their **CB[7]** complexes, where the iodine atom was replaced with an ethynyl-aryl-pyridinium moiety.

Importantly, the isomerization rates and activation enthalpies remained nearly unchanged upon complexation with **CB[7]**, suggesting that the photoswitchable units are spatially decoupled from the **CB[7]** binding site and retain their intrinsic photochemical behavior.

In the next step, all four complexes **1–4·CB[7]**, along with **CB[7]** alone and **9·CB[7]** as references, were adsorbed onto gold surfaces. Self-assembled monolayers (SAMs) composed of **CB[7]** were formed by immersing the gold substrates in a 0.5 mM aqueous solution for 20 hours. The complexes were subsequently adsorbed from 0.1 mM DMSO solutions over a period of 48 to 72 hours. Importantly, at these concentrations the 1 : 1 **CB[7]** complexes remain fully stable in solution, and no measurable dissociation occurs during the adsorption process. All resulting samples were analyzed using contact angle goniometry, ellipsometry, PM-IRRAS, surface-enhanced Raman spectroscopy (SERS), UV-vis spectroscopy, and atomic force microscopy (AFM), with the results discussed in the following sections.

Surface hydrophilicity was evaluated using water contact angle goniometry. Measured values ranged approximately between 40–50° (see SI for details), as summarized in Table 2. The observed increase in contact angle relative to the neat, freshly annealed gold substrate (14 ± 2°), as well as substrates immersed in DMSO (22 ± 3°), confirms the formation of an organic layer on the surface.

Ellipsometry offered additional indirect evidence for the presence of surface-adsorbed molecular layers. Measurements indicated that complexes **1–4·CB[7]** and **9·CB[7]** formed films approximately 16 Å thick, whereas neat **CB[7]**, likely oriented horizontally, yielded thinner films around 11 Å. These values are in reasonable agreement with theoretical predictions (Table 2), especially considering the limitations of ellipsometry.[32] This technique averages measurements over relatively large surface areas, depends heavily on the assumed refractive index of the film, and is generally known to underestimate actual monolayer thicknesses.[30]

AFM scratching experiments enabled more precise determination of monolayer thicknesses (see Table 2). In this method, the AFM tip mechanically removed the adsorbed layer from a localized region of the gold substrate, allowing direct measurement of the height difference between the exposed surface and the surrounding intact monolayer. The measured thicknesses closely matched the theoretically predicted heights h, based on the expected molecular orientations shown in Fig. 4B. These data also reflected the relative lengths of the molecular rods: the longest complexes, **1–2·CB[7]**, formed films approximately 24 Å thick (theoretical ~26 Å), while the shorter complexes **4·CB[7]** and **9·CB[7]** yielded films around 19 Å

Table 2 Preparation and characterization of SAMs made of complexes **1–4·CB[7]**, **9·CB[7]**, and **CB[7]** alone

Sample	Immer. time (h)	Contact angle (°)	Ellips. thickness (Å)	Layer thickness by AFM (Å)	Length of the guest (Å)	Theor. layer height *h* (Å)
1·CB[7]	72	50 ± 4	15 ± 2	23 ± 2	26	25
2·CB[7]	48	45 ± 2	16 ± 1	24 ± 3	27	26
3·CB[7]	48	40 ± 4	13 ± 2	15 ± 2	21	20
4·CB[7]	48	47 ± 2	18 ± 1	18 ± 1	21	20
9·CB[7]	48	40 ± 4	17 ± 2	20 ± 2	19	18
CB[7]	18	52 ± 4	11 ± 1	10 ± 1	N/A	9

(theoretical ~19 Å). Bare **CB[7]** formed the thinnest layer, ~10 Å, consistent with the expected ~9 Å for a horizontally aligned macrocycle (see SI for more details). The only notable discrepancy was observed for complex **3·CB[7]**, which consistently produced films of 15 ± 2 Å, roughly 5 Å shorter than the expected 20 Å. This deviation may result from additional bending of the molecule, potentially due to interactions between the nitrile group in the diazocine unit and the gold surface.

The presence of characteristic vibrational modes associated with specific functional groups (particularly the C=O and C–N stretching vibrations) in **1–4·CB[7]**, **9·CB[7]**, and **CB[7]** was clearly confirmed by PM-IRRAS spectroscopy. In addition, samples containing **1·CB[7]** and **CB[7]** were further analyzed using surface-enhanced Raman spectroscopy (SERS). Representative spectra of **1·CB[7]** obtained by both PM-IRRAS and SERS are shown in Fig. 6, while data for the other samples are provided in the SI.

The PM-IRRAS spectrum of **1·CB[7]** adsorbed from DMSO displayed a prominent absorption bands near 1750 and 1470 cm^{-1}, which were attributed to the carbonyl and C–N stretching vibrations of the **CB[7]** macrocycle (Fig. 5).[21] Notably, vibrations typically associated with the guest molecule - such as the asymmetric stretching of the C≡C triple bond or the nitrile group, both expected around 2200 cm^{-1} based on isotropic KBr pellet spectra - were not detected. This absence can be attributed to the dominant intensity of **CB[7]** bands, which overshadow the comparatively weaker guest signals due to **CB[7]**'s high symmetry and the presence of 14 equivalent carbonyl groups. Nonetheless, the persistence of strong carbonyl bands characteristic of **CB[7]**, combined with the known stability of **CB[7]** complexes in solution, supports the conclusion that **1·CB[7]** is indeed present on the gold surface.

Owing to the distinct selection rules of Raman spectroscopy, vibrational modes that appear strongly in IR spectra - such as the carbonyl stretching of **CB[7]** - are less intense or even suppressed in Raman spectra. This attenuation of **CB[7]** signals in the Raman spectrum enabled the detection of vibrational bands attributed to the guest molecule within the complex. Specifically, bands corresponding to the C≡C triple bond stretching (~2200 cm^{-1}) and aromatic ring stretching modes (1508 cm^{-1}, 1570 cm^{-1}, and 1604 cm^{-1}) were clearly observed alongside weaker **CB[7]** bands in the Raman spectrum of powdered **1·CB[7]** (Fig. 6). Additionally, the SERS of **1·CB[7]** adsorbed onto a gold surface was acquired (Fig. 6), with distinct bands attributable to the complex. These observations further support the presence of **1·CB[7]** on the gold surface.

A central question was whether the surface-anchored complexes retain their ability to undergo photoisomerization. To address this, UV–vis absorption spectroscopy was carried out on SAMs of **1–4·CB[7]** prepared on semi-transparent gold films (~5 nm Au on silylated quartz).[15,33,34] In all cases, irradiation induced the characteristic spectral changes associated with

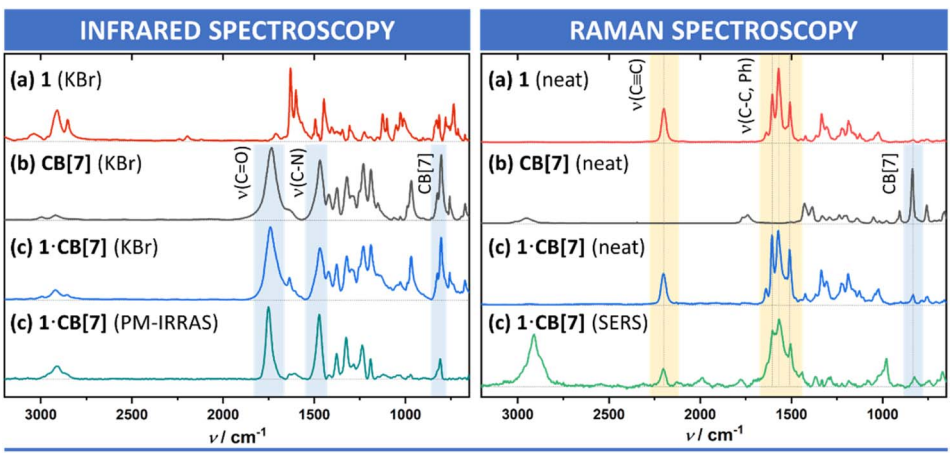

Fig. 6 Left: Isotropic IR spectra of (a) neat guest **1**, (b) **CB[7]**, and (c) the **1·CB[7]** complex recorded in KBr pellets, along with (d) the anisotropic PM-IRRAS spectrum of **1·CB[7]** adsorbed on an Au(111) surface. Right: Raman spectra of (a) neat guest **1**, (b) **CB[7]** and (c) **1·CB[7]** and (d) SERS of **1·CB[7]** adsorbed on gold surface.

photoisomerization, followed by thermal and/or photoinduced relaxation (Fig. S51–S57). These surface-based differential spectra closely mirror the behavior observed in solution, where the photoisomerization is unambiguously confirmed by combined NMR and UV-vis spectroscopy. Fig. 7 illustrates a representative example for the azobenzene **2·CB[7]** SAM. Because of the inherently low signal-to-noise ratio of surface UV-vis measurements, the data are presented as differential spectra collected before and after UV irradiation. Upon excitation at 400 ± 5 nm, the broad absorption band at ~390 nm corresponding to π–π* transition decreases, yielding a negative differential feature consistent with *trans*-to-*cis* conversion (Fig. 7B). Subsequent thermal relaxation restores the original spectrum (Fig. 7D), in full agreement with the solution behavior (Fig. 7A and C).

Kinetic analysis performed for SAMs of **1–3·CB[7]** (see SI for additional details) afforded half-lives comparable to those in solution (Table 1). For **3·CB[7]**, the surface spectra exhibit only modest amplitude changes, a consequence of its inherently lower molar absorptivities in both isomeric states. Nonetheless, the qualitative photoswitching behavior closely matches the solution data, supporting reliable surface photoisomerization.

To quantify the packing density, the surface coverage of the **CB[7]**-based SAMs was determined using two independent approaches: AFM counting of individual **CB[7]** units and UV-vis absorbance analysis (see SI). Both methods yielded consistent values of *ca.* 60% (±10–15%), in good agreement with the incomplete monolayer coverage typically reported for **CB[7]** on gold.[23,35] The agreement between the two measurements supports the robustness of the SAM preparation and confirms reliable surface attachment of the photoactive complexes.

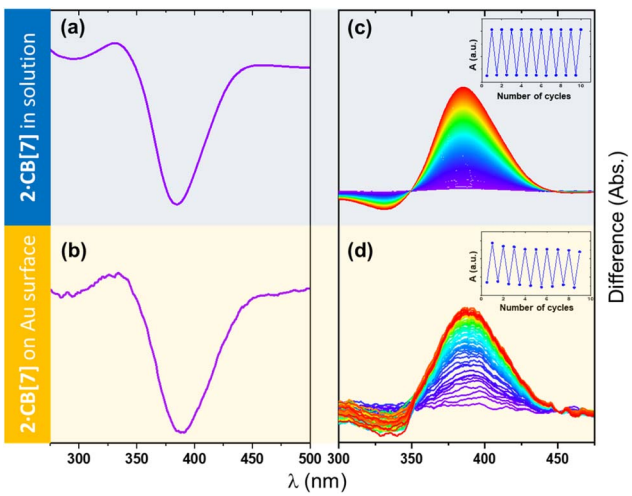

Fig. 7 Differential UV-vis absorption spectra of **2·CB[7]** in DMSO solution (a) and within a self-assembled monolayer (SAM) on a gold substrate (b) before and after photoirradiation at 400 ± 5 nm, recorded at 20 °C in solution and 15 °C in the SAM. Panels (c) and (d) display the corresponding thermal relaxation of **2·CB[7]** at 30 °C in solution and 40 °C in the SAM. Insert: Stability of **2·CB[7]** in solution and in the SAM upon alternating irradiation with 400 nm light (6 min in solution; 25 s in SAM, using 70% light intensity) and 450 nm light (1 min in solution; 15 s in SAM, using 50% light intensity).

These observations not only provided further confirmation of the successful immobilization of the complexes on the gold surface but, more importantly, demonstrated the preserved photoactivity of the surface-bound layers. The results also indicate that the molecular anchor effectively decouples the photoresponsive unit from the gold substrate, thereby preventing quenching of the excited state and allowing efficient photoisomerization.

Conclusions

A series of four photoswitchable molecular rods (**1–4**) were synthesized and complexed with **CB[7]** to form supramolecular assemblies **1–4·CB[7]**. The complexation was followed by ^{1}H NMR spectroscopy. Photochemical studies revealed that the complexes retained the switching behavior of the parent compounds, with minimal impact from **CB[7]** encapsulation, indicating spatial decoupling of the photoactive core from the binding site.

The complexes were immobilized on gold surfaces as self-assembled monolayers (SAMs) and characterized by ellipsometry, AFM, PM-IRRAS, and SERS, confirming their presence and structural integrity. Importantly, the SAMs of all four complexes **1–4·CB[7]** exhibited fully reversible photoisomerization upon UV irradiation, clearly demonstrating preserved photoactivity on the surface. These results underline the effectiveness of the molecular architecture in enabling surface-confined photoswitching, offering a robust platform for photoresponsive functional interfaces.

Author contributions

D. L. carried out synthesis and characterization of molecular rods and complexes and performed UV-vis characterization of photoswitches in solution. E. K. performed AFM and UV-vis analysis of SAMs. K. M. V., C. S. H. and M. M. prepared and characterized SAMs. I. C. determined all single-crystal X-ray diffraction structures. J. K. conceived the project.

Conflicts of interest

There are no conflicts to declare.

Data availability

CCDC 2457321 (compound **8**) and 2457322 (compound **2**) contain the supplementary crystallographic data for this paper.[36a,b]

The data supporting this article have been included as part of the supplementary information (SI). Supplementary information: synthetic procedures, copies of ^{1}H and ^{13}C NMR spectra of all new derivatives, UV-vis analysis of photoswitching and thermal steps in solution and within SAMs (**1–4**, **1–4·CB[7]**, **10–13**), ^{1}H NMR analysis of photoswitching (**2–4** and **10–13**), quantum yield determination (**3** and **4**), preparation of gold substrates, characterization of SAMs (AFM visualizations and scratching experiments, ellipsometry, contact angle

goniometry, PM-IRRAS, Raman, photoswitching monitored by UV-vis), and ORTEP views of single molecule and packing in two crystal structures (**2** and **8**), are available in the Supporting Information file (PDF). Optimized geometries of **1–4**·**CB[7]** (xyz). See DOI: https://doi.org/10.1039/d5sc09469k.

Acknowledgements

This work was supported by the Institute of Organic Chemistry and Biochemistry, Academy of Sciences of the Czech Republic (RVO: 61388963), Czech Science Foundation (grant number: 25–16074S), and the Ministry of Education, Youth and Sports (grant number: LTAUSA19120). We are grateful to Dr Lucie Bednárová for help with IR spectra, Dr Anna Šemberová for help with Raman spectra, Dr Lukáš Severa for performing calculations, and Dr Jakub Radek Štoček and Dr Martin Dračínský for help with assigning NMR spectra. Finally, we are grateful to Prof. Eric Masson for providing the **CB[7]** macrocycle.

References

1 A. Goulet-Hanssens, F. Eisenreich and S. Hecht, *Adv. Mater.*, 2020, **32**(20), 1905966.
2 J. Kaleta, Molecular Switches and Motors in 2-D, in *Molecular Photoswitches*, ed. Z. L. Pianowski, Wiley-VCH GmbH, 2022.
3 R. Klajn, *Pure Appl. Chem.*, 2010, **82**, 2247–2279.
4 Y. Deng, G. Long, Y. Zhang, W. Zhao, G. Zhou, B. L. Feringa and J. Chen, *Light:Sci. Appl.*, 2024, **13**(1), 63.
5 H. Chen and J. F. Stoddart, *Nat. Rev. Mater.*, 2021, **6**, 804–828.
6 T. Li, V. K. Bandari and O. G. Schmidt, *Adv. Mater.*, 2023, **35**, 2209088.
7 M. Valášek and M. Mayor, *Chem. Eur. J.*, 2017, **23**, 13538–13548.
8 K.-Y. Chen, O. Ivashenko, G. T. Carroll, J. Robertus, J. C. M. Kistemaker, G. London, W. R. Browne, P. Rudolf and B. L. Feringa, *J. Am. Chem. Soc.*, 2014, **136**, 3219–3224.
9 R. Löw, T. Rusch, F. Röhrlich, O. Magnussen and R. Herges, *Beilstein J. Org.Chem.*, 2019, **15**, 1485–1490.
10 B. Baisch, D. Raffa, U. Jung, O. M. Magnussen, C. Nicolas, J. Lacour, J. Kubitschke and R. Herges, *J. Am. Chem. Soc.*, 2009, **131**, 442–443.
11 L. Severa, C. Santos Hurtado, I. Rončević, M. Mašát, G. Bastien, J. R. Štoček, M. Dračínský, V. Houska, E. Kaletová, D. J. Garza, I. Císařová, K. L. A. Cimatu, Z. Bastl and J. Kaleta, *Chem. Eur. J.*, 2024, **30**, e2023028.
12 G. Bastien, L. Severa, M. Škuta, C. Santos Hurtado, J. Rybáček, V. Šolínová, I. Císařová, V. Kašička and J. Kaleta, *Chem. Eur. J.*, 2024, **30**, e202401889.
13 F. Ishiwari, G. Nascimbeni, H. Tago, Y. Shoji, S. Fujii, M. Kiguchi, T. Tada, M. Zharnikov, E. Zojer and T. Fukushima, *J. Am. Chem. Soc.*, 2019, **141**, 5995–6005.
14 S. Das, F. Ishiwari, Y. Shoji, T. Fukushima and M. Zharnikov, *J. Phys. Chem. C*, 2023, **127**, 5178–5185.
15 K. Bezděková, L. Severa, E. Kaletová, K. Majerová Varga, M. Mašát, L.-T. Wu, J.-C. Jiang, I. Císařová and J. Kaleta, *Angew. Chem., Int. Ed.*, 2025, **65**, e202513922.
16 F. Tian, D. Jiao, F. Biedermann and O. A. Scherman, *Nat. Commun.*, 2012, **3**(1), 1207.
17 C. Santos Hurtado, G. Bastien, I. Rončević, M. Dračínský, E. Tortorici, C. Rogers, J. Michl and J. Kaleta, *Chem. Comm.*, 2024, **60**, 960–963.
18 C. Santos Hurtado, G. Bastien, M. Mašát, J. R. Štoček, M. Dračínský, I. Rončević, I. Císařová, C. T. Rogers and J. Kaleta, *J. Am. Chem. Soc.*, 2020, **142**, 9337–9351.
19 J. Kaleta, J. Chen, G. Bastien, M. Dračínský, M. Mašát, C. T. Rogers, B. L. Feringa and J. Michl, *J. Am. Chem. Soc.*, 2017, **139**, 10486–10498.
20 K. Kim, W. S. Jeon, J.-K. Kang, J. W. Lee, S. Y. Jon, T. Kim and K. Kim, *Angew. Chem., Int. Ed.*, 2003, **42**(20), 2293–2296.
21 L. Qi, H. Tian, H. Shao and H.-Z. Yu, *J. Phys. Chem. C*, 2017, **121**(14), 7985–7992.
22 A. Corma, H. García, P. Montes-Navajas, A. Primo, J. J. Calvino and S. Trasobares, *Chem. - Eur. J.*, 2007, **13**(22), 6359–6364.
23 Q. An, G. Li, C. Tao, Y. Li, Y. Wu and W. Zhang, *Chem. Commun.*, 2008, **17**, 1989.
24 E. Blanco, C. Quintana, L. Hernández and P. Hernández, *Electroanalysis*, 2013, **25**(1), 263–268.
25 A. Gomez-Casado, P. Jonkheijm and J. Huskens, *Langmuir*, 2011, **27**(18), 11508–11513.
26 S. Liu, C. Ruspic, P. Mukhopadhyay, S. Chakrabarti, P. Y. Zavalij and L. Isaacs, *J. Am. Chem. Soc.*, 2005, **127**(45), 15959–15967.
27 D. Lončarić, F. Movahedifar, J. R. Štoček, M. Dračínský, J. Cvačka, G. Shanshan, B. Bythell, I. Císařová, E. Masson and J. Kaleta, *Chem. Sci.*, 2023, **14**, 9258–9266.
28 S. Grimme, C. Bannwarth and P. J. Shushkov, *Chem. Theory Comput.*, 2017, **13**, 1989–2009.
29 C. Bannwarth, S. Ehlert and S. Grimme, *J. Chem. Theory Comput.*, 2019, **15**, 1652–1671.
30 S. Grimme, *J. Chem. Theory Comput.*, 2019, **15**, 2847–2862.
31 C. Santos Hurtado, G. Bastien, D. Lončarić, M. Dračínský, I. Císařová, E. Masson and J. Kaleta, *Chem. Sci.*, 2025, **16**, 14081–14087.
32 H. Fujiwara, Effect of Roughness on Ellipsometry Analysis, in *Spectroscopic Ellipsometry for Photovoltaics*, ed. Fujiwara H. and Collins R., Springer Series in Optical Sciences. Springer, Cham, 2018, 212.
33 J. Chen, K.-Y. Chen, G. T. Carroll and B. L. Feringa, *Chem. Commun.*, 2014, **50**, 12641–12644.
34 K.-Y. Chen, S. J. Wezenberg, G. T. Carroll, G. London, J. C. M. Kistemaker, T. C. Pijper and B. L. Feringa, *J. Org. Chem.*, 2014, **79**, 7032–7040.
35 A. Gomez-Casado, P. Jonkheijm and J. Huskens, *Langmuir*, 2011, **27**(18), 11508–11513.
36 (*a*) CCDC 2457321: Experimental Crystal Structrue Determination, 2026, DOI: 10.5517/ccdc.csd.cc2nh1fn.; (*b*) CCDC 2457322: Experimental Crystal Structrue Determination, 2026, DOI: 10.5517/ccdc.csd.cc2nh1gp.